

Efficient Spin-Orbit Torque Generation in Semiconducting WTe₂ with Hopping Transport

Cheng-Wei Peng,^{1,a)} Wei-Bang Liao,^{1,a)} Tian-Yue Chen,¹ and Chi-Feng Pai^{1,2,b)}

¹Department of materials science and engineering, National Taiwan University, Taipei 10617, Taiwan

²Center of Atomic initiative for new materials, National Taiwan University, Taipei 10617, Taiwan

^{a)}These authors contributed equally to this work.

^{b)}Author to whom correspondence should be addressed: Email: cfpai@ntu.edu.tw

Abstract

Spin-orbit torques (SOTs) from transition metal dichalcogenides systems (TMDs) in conjunction with ferromagnetic materials are recently attractive in spintronics for their versatile features. However, most of the previously studied crystalline TMDs are prepared by mechanical exfoliation, which limits their potentials for industrial applications. Here we show that amorphous WTe₂ heterostructures deposited by magnetron sputtering possess a sizable damping-like SOT efficiency $\xi_{DL}^{WTe_2} \approx 0.20$ and low damping constant $\alpha = 0.009 \pm 0.001$. Only an extremely low critical switching current density $J_c \approx 7.05 \times 10^9$ A/m² is required to achieve SOT-driven magnetization switching. The SOT efficiency is further proved to depend on the W and Te relative compositions in the co-sputtered W_{100-x}Te_x samples, from which a sign change of $\xi_{DL}^{WTe_2}$ is observed. Besides, the electronic transport in amorphous WTe₂ is found to be semiconducting and is governed by a hopping mechanism. With the above advantages and rich tunability, amorphous and semiconducting WTe₂ serves as a unique SOT source for future spintronics applications.

Keywords: Transition metal dichalcogenide, spin-orbit torque, spintronics, damping constant

I. Introduction

With the advancement of spintronics and next generation magnetic random access memory (MRAM) technologies, spin-orbit torques (SOTs) originated from the spin-orbit interactions in various types of materials systems and magnetic heterostructures have been shown to be an effective mechanism to manipulate and switch the magnetization similar to or more efficient than the traditional spin-transfer torque (STT) approach.¹⁻⁴ When it comes to materials with sizable efficiency of generating spin current from charge current, the 5d transition metals like Pt,^{1,2} Ta,⁵ and W⁶⁻⁹ are the typically chosen due to the strong spin-orbit coupling (SOC) therein, which can induce spin currents and SOTs through the spin Hall effect (SHE).^{5,10,11}

More recently, topological insulators (TIs) such as BiSe,¹²⁻¹⁵ BiSb,¹⁶ and $(\text{Bi}_{0.5}\text{Sb}_{0.5})_2\text{Te}_3$ ¹⁷ are reported to possess high SOT efficiency from spin momentum locking of topologically-protected surface states (TSSs). Interestingly, various non-epitaxial Bi-based chalcogenides without TSS have also been reported to show giant SOT efficiencies.¹⁸⁻²⁰ Another family of emergent materials, transition metal dichalcogenides (TMDs), have also gained lots of attention due to not only the strong SOC but also their unconventional SOT features from the lack of inversion symmetry.²¹⁻³² These unique properties lead to the possibility of electric field control over SOT²⁴ and generation of out-of-plane damping-like (DL) SOTs.^{22,23,25,28,30} Particularly, for exfoliated WTe₂, MacNeill *et al.* confirmed the existence of anomalous DL-SOT in WTe₂/Py through spin-torque ferromagnetic resonance (ST-FMR) measurements.²² Li *et al.* observed an enhanced spin conductivity in WTe₂/Py originated from spin momentum locking.²⁶ Shi *et al.* reported an extremely large DL-SOT efficiency up to 0.5 for WTe₂/Py, which was attributed to a bulk origin.²⁷ Although all these studies suggest that WTe₂ is a promising SOT material with rich tunability, most of them require mechanical exfoliation of single-crystalline WTe₂, which is of great challenge to realize in mass production. It is therefore crucial to explore the possibilities of employing WTe₂ layers prepared by conventional materials growth approaches, such as magnetron sputter deposition, to see their spin transport properties as compared to the

exfoliated cases.

In this work, we report the DL-SOT efficiencies from both stoichiometric WTe_2 and co-sputtered $\text{W}_{100-x}\text{Te}_x$ -based magnetic heterostructures prepared by high vacuum sputter depositions. Both series of deposited multilayer stacks are amorphous. We first quantify the damping constant of $\text{WTe}_2/\text{CoFeB}$ devices with in-plane magnetic anisotropy (IMA) through ST-FMR measurements,³³ from which the damping constant is determined to be $\alpha_{\text{WTe}_2/\text{CoFeB}} = 0.009 \pm 0.001$, smaller than those from the transition metal-based control samples, namely $\alpha_{\text{W/CoFeB}} \approx 0.014$ and $\alpha_{\text{Pt/CoFeB}} \approx 0.033$. The largest DL-SOT efficiency from the stoichiometric WTe_2/CoTb devices with perpendicular magnetic anisotropy (PMA) is further estimated to be $\xi_{\text{DL}}^{\text{WTe}_2} \approx 0.20$ by current-induced hysteresis loop shift measurement.³⁴ Current-induced magnetization switching at a low critical switching current density $J_c \approx 7.05 \times 10^9 \text{ A/m}^2$ further confirms the sizable DL-SOT efficiency. By studying the co-sputtered $\text{W}_{100-x}\text{Te}_x$ samples, we find that $\xi_{\text{DL}}^{\text{W}_{100-x}\text{Te}_x}$ is strongly composition dependent in terms of both magnitude and sign, which can explain the huge discrepancies of observed ξ_{DL} in several recent reports.^{35,36} Additionally, the distinct difference between the layer thickness dependence of $\xi_{\text{DL}}^{\text{WTe}_2}$ and $\xi_{\text{DL}}^{\text{W}_{100-x}\text{Te}_x}$ suggests that both bulk and interfacial origins of SOTs are possible to be generated by sputter-deposited chalcogenides. These unconventional features together with its low α and sizable ξ_{DL} , make amorphous WTe_2 -based heterostructure an intriguing system for novel SOT applications.

II. Materials and Methods

The samples in this work are all prepared by magnetron sputtering and deposited onto thermally oxidized silicon substrates with base pressure $\sim 3 \times 10^{-8}$ Torr. We use dc sputtering for metallic targets under 3 mTorr of Ar working pressure, while MgO target is rf sputtered

under 10 mTorr of Ar working pressure. Three series of samples are prepared, namely $\text{WTe}_2(10)/\text{CoFeB}(5)/\text{MgO}(1)/\text{Ta}(1)$ for ST-FMR measurements, $\text{WTe}_2(t)/\text{CoTb}(6)/\text{Ta}(2)$ for hysteresis loop shift and current-induced magnetization switching measurements, and co-sputtered $\text{W}_{100-x}\text{Te}_x(10)/\text{CoTb}(4.5)/\text{Ta}(2)$ (units in nanometers) for further comparisons. The WTe_2 layer is deposited directly from a stoichiometric WTe_2 target, while the CoFeB layer is sputtered from a $\text{Co}_{40}\text{Fe}_{40}\text{B}_{20}$ target. The $\text{Co}_{55}\text{Tb}_{45}$ (CoTb) layer and $\text{W}_{100-x}\text{Te}_x$ layer are deposited by co-sputtering Co and Tb targets as well as W and Te targets, respectively. Note that WTe_2 layer is grown at a substrate temperature of 300°C to ensure the uniformity.³⁷ The thicknesses of each layer are checked by atomic force microscopy (AFM). Electron probe X-ray microanalyzer (EPMA) is employed to confirm the atomic ratios of the sputtered WTe_2 and co-sputtered $\text{W}_{100-x}\text{Te}_x$ thin films. For further electrical measurements, the films are patterned into microstrip with lateral dimensions of $40\ \mu\text{m}\times 100\ \mu\text{m}$ for ST-FMR measurement and Hall bar devices with lateral dimensions of $10\ \mu\text{m}\times 60\ \mu\text{m}$ for hysteresis loop shift and current-induced magnetization switching measurements through standard photolithography and followed by Ar ion-milling.

III. Results

A. Materials characterizations

The structural properties of the sputtered WTe_2 films are first examined by cross-sectional field-emission transmission electron microscopy (FE-TEM, JEOL 2010F). The TEM sample is prepared by a lift-out technique with SEIKO SMI-3050SE focused ion beam (FIB). As shown in Fig. 1(a), the sputtered WTe_2 in a representative $\text{WTe}_2(10)/\text{CoFeB}(5)/\text{MgO}(1)/\text{Ta}(1)$ sample is amorphous. Figure 1(b) shows the normalized secondary ion mass spectrometer (SIMS) signals from the same thin film during Ar ion-milling process. The peaks of Mg, Co, W, and Te correspond to the signals from the MgO layer, the CoFeB layer, and the WTe_2 layer being etched, respectively. According to the EPMA analysis, the atomic ratio between W and Te are 33% and

67% in our sputtered WTe₂ films, therefore we keep the stoichiometric notation of WTe₂ to represent samples deposited from the WTe₂ target (see the supplementary material S1). The resistivities of each material are measured by four-point probe measurement, among which $\rho_{\text{WTe}_2} \approx 1870 \mu\Omega\text{-cm}$ (see the supplementary material S2). We further examine the electrical transport properties by measuring the temperature dependence of resistivity from 323 K to 423 K, which suggests our sputtered WTe₂ and W_{100-x}Te_x films are semiconducting rather than metallic (see the supplementary material S3).

We further examine the electrical transport properties by measuring the temperature dependence of resistivity from 323 K to 423 K. Most of the previous works claimed that the textured WTe₂ is one kind of Weyl semimetal,^{26,27} while our sample is predominately amorphous and therefore should not fall into this category. According to the electrical transport measurement shown in supplementary material S3, the sputtered amorphous WTe₂ is semiconducting and the temperature dependent resistivity can be well described by small polaron hopping (SPH) model,³⁸ where the thermally-activated hopping polarons from electron-phonon interaction dominate the electrical transport.

B. ST-FMR measurement

We then investigate the spin transport properties of WTe₂(10)/CoFeB(5)/MgO(1)/Ta(1) with ST-FMR. CoFeB is chosen to be the ferromagnetic (FM) layer because it is widely used in contemporary MTJs.^{1,39,40} MgO(1)/Ta(1) layers are employed to prevent the layers beneath from oxidation. In a typical ST-FMR measurement, a rf current is applied, generating a rf spin current from the SOC buffer layer (WTe₂) to induce the precessional magnetization of the FM layer, which leads to an oscillation of the resistance owing to the anisotropic magnetoresistance. With the mixing of oscillating resistance and rf current, we can measure a rectified dc voltage V_{mix} of the device through a bias tee, as illustrated in Fig. 2(a). A rf current is generated from

the signal generator with the amplitude modulated at 500 Hz, which allows the use of lock-in amplifier for V_{mix} detection. A sweeping in-plane field H_{ext} is applied at a fixed angle of 135° between H_{ext} and the current channel. Typical field-swept ST-FMR spectra of a $\text{WTe}_2(10)/\text{CoFeB}(5)$ microstrip under frequencies of $f = 7$ to 12 GHz are shown in Fig. 2(b). The spectrum of $f = 10$ GHz is further scrutinized in Fig. 2(c), in which the data points of V_{mix} can be fitted with³³

$$V_{\text{mix}} = S \frac{\Delta^2}{\Delta^2 + (H_{\text{ext}} - H_0)^2} + A \frac{\Delta(H_{\text{ext}} - H_0)}{\Delta^2 + (H_{\text{ext}} - H_0)^2}, \quad (1)$$

where S , A , Δ , and H_0 denote symmetric Lorentzian coefficient, anti-symmetric Lorentzian coefficient, linewidth, and resonant field, respectively. The symmetric part of V_{mix} originates from the in-plane DL torque (τ_{\parallel}), while the anti-symmetric part comes from the out-of-plane field-like (FL) torque (τ_{\perp}) and the Oersted field. The torque ratio is further evaluated by^{24,33}

$$\frac{\tau_{\parallel}}{\tau_{\perp}} = \frac{S}{A} \sqrt{1 + \frac{4\pi M_{\text{eff}}}{H_0}}, \quad (2)$$

where $4\pi M_{\text{eff}} \approx 11.7$ kOe is the demagnetization field extracted from the fitting of Kittel formula (see the supplementary material S4). Note that the contribution from the Oersted field is negligible in our system. For the $\text{WTe}_2(10)/\text{CoFeB}(5)$ device, the torque ratio is 2.75 ± 0.54 , which indicates a considerable DL torque contribution. However, in ST-FMR measurement, other factors like the FM thicknesses dependent FL-SOT^{41,42} and spin-pumping effect^{43,44} might plague the estimation of $\xi_{\text{DL}}^{\text{WTe}_2}$ from torque ratio. Therefore, we choose to quantify $\xi_{\text{DL}}^{\text{WTe}_2}$ via other approaches, which will be addressed in the following section.

Nevertheless, ST-FMR provides us other valuable information, such as damping constant

α , which is one of the key figures of merit to realize efficient current-induced switching.^{45,46} α can be estimated from $\Delta = \Delta_0 + \frac{2\pi\alpha}{\gamma} f$, where Δ_0 is the linewidth from inhomogeneous broadening, and γ is the gyromagnetic ratio. Figure 2(d) shows the linewidths as functions of frequencies of WTe₂, Pt and W-based magnetic heterostructures. Surprisingly, the WTe₂(10)/CoFeB(5) device shows $\alpha_{\text{WTe}_2/\text{CoFeB}} = 0.009 \pm 0.001$, which is smaller than those obtained from control samples with classical spin Hall transition metals, namely Pt(6)/CoFeB(5) ($\alpha_{\text{Pt/CoFeB}} = 0.033 \pm 0.003$) and W(4)/CoFeB(5) ($\alpha_{\text{W/CoFeB}} = 0.014 \pm 0.002$). Note that $\alpha_{\text{WTe}_2/\text{CoFeB}}$ from our sputtered WTe₂/CoFeB is comparable to those observed from exfoliated WTe₂/Py heterostructures.^{22,27}

C. Hysteresis loop shift measurement

Next, we employ hysteresis loop shift measurement³⁴ to quantify the DL-SOT efficiency $\xi_{\text{DL}}^{\text{WTe}_2}$ of WTe₂/FM heterostructures, with FM being ferrimagnetic CoTb alloy with PMA. Ferrimagnets are widely used as SOT detector due to their robust bulk PMA on diverse materials with SOC.^{13,47,48} The setup for loop shift measurement on a WTe₂(10)/CoTb(6)/Ta(2) Hall bar device with suitable PMA ($H_c \approx 60$ Oe) is depicted in Fig. 3(a). A dc current (I_{dc}) is applied along the current channel with a parallel in-plane bias field H_x . With H_x overcoming the effective field from interfacial Dzyaloshinskii-Moriya interaction (DMI) H_{DMI} and realigning the domain wall moments, the current-induced effective field from DL-SOT will assist domain wall propagation and domain expansion.^{49,50} When $|H_x| \geq |H_{\text{DMI}}|$, the current-induced DL-SOT from WTe₂ can fully act on the domain wall moments of CoTb and it can be seen as an out-of-plane effective field H_z^{eff} causing the hysteresis loop to shift. This can be monitored via anomalous Hall voltage measurements, as shown in Fig. 3(b). By obtaining the slope of H_z^{eff} vs I_{dc} , as shown in Fig. 3(c), the DL-SOT efficiency (ξ_{DL}) can be estimated through³⁴

$$\xi_{\text{DL}} = \frac{2e}{\hbar} \left(\frac{2}{\pi} \right) \mu_0 M_s t_{\text{CoTb}} w t_{\text{WTe}_2} \left(\frac{\rho_{\text{CoTb}} t_{\text{WTe}_2} + \rho_{\text{WTe}_2} t_{\text{CoTb}}}{\rho_{\text{CoTb}} t_{\text{WTe}_2}} \right) \left(\frac{H_z^{\text{eff}}}{I_{\text{dc}}} \right), \quad (3)$$

where $M_s \approx 48 \text{ emu/cm}^3$ is the saturation magnetization of the CoTb layer (characterized by vibrating sample magnetometer (VSM)), $w = 10 \text{ }\mu\text{m}$ is the width of the Hall bar device, and ρ represents the layer resistivity. The estimated DL-SOT efficiency of the sputtered WTe₂(10)/CoTb(6) heterostructure is $\xi_{\text{DL}}^{\text{WTe}_2} \approx 0.20$, which is comparable with the exfoliated crystalline WTe₂/FM.^{27,31} It is worth noting that this sizable $\xi_{\text{DL}}^{\text{WTe}_2}$ is in sharp contrast to a recent work by Fan *et al.*, in which a relatively small $\xi_{\text{DL}} \approx -0.0021$ but a large $\xi_{\text{FL}} \approx 0.057$ are reported for the sputtered W_xTe_{2-x}.³⁵ Figure 3(d) shows $H_z^{\text{eff}} / I_{\text{dc}}$ ($\propto \xi_{\text{DL}}$) as a function of H_x for WTe₂/CoTb and W/CoTb (control sample) devices. It can be observed that the signs of $H_z^{\text{eff}} / I_{\text{dc}}$ for the two devices are opposite ($\xi_{\text{DL}}^{\text{WTe}_2} > 0$ and $\xi_{\text{DL}}^{\text{W}} < 0$), which is consistent with the exfoliated WTe₂ case.^{22,27,31} We emphasize that both the DL effective field ($H_z^{\text{eff}} / I_{\text{dc}}$) and the estimated DL-SOT efficiency of WTe₂-based device ($\xi_{\text{DL}}^{\text{WTe}_2} \approx 0.20$) are greater than those of the W-based control sample ($\xi_{\text{DL}}^{\text{W}} \approx -0.04$) (see the supplementary material S5). It is also interesting to note that $|H_{\text{DMI}}^{\text{WTe}_2}| \gg |H_{\text{DMI}}^{\text{W}}|$, which suggests that the WTe₂-based device might have a stronger interfacial SOC than the W-based case.

D. Current-induced magnetization switching

We further demonstrate current-induced SOT-driven magnetization switching in WTe₂(10)/CoTb(6)/Ta(2) magnetic heterostructures. Pulsed currents are injected into the current channel of Hall bar devices, and again, an H_x is applied to overcome H_{DMI} such that

the deterministic magnetization switching can be achieved. As shown in Fig. 4(a), the switching polarities depend on the applied H_x , which is consistent with the SOT-driven switching mechanism.^{2,5} More importantly, the critical switching current density J_c of WTe₂/CoTb structure is further demonstrated to be $J_c \approx 7.05 \times 10^9 \text{ A/m}^2$, which is much lower than those from the 5d transition metal-based heterostructures ($J_c \approx 10^{11} \text{ A/m}^2$)^{1,5,6} and comparable to the TI cases.¹³⁻¹⁶ Note that this value is of the same order as the exfoliated 80 nm-thick-WTe₂ case reported by Shi. S *et al.* ($J_c \approx 3 \times 10^9 \text{ A/m}^2$),²⁷ and smaller than the sputtered WTe_x case reported by Li *et al.* ($J_c \approx 1.5 \times 10^{10} \text{ A/m}^2$).³⁶ In addition to J_c , the SOC layer thickness also needs to be taken into account to estimate the overall switching performance. We evaluate the ideal critical switching current through $I_c^{\text{ideal}} = J_c (t \cdot w)$, where t is the required SOC buffer layer thickness and w is the ideal current channel width assumed to be 100 nm. Figure 4(b) compares the reported J_c and estimated I_c^{ideal} from several TIs and WTe_x-based magnetic heterostructures (see the supplementary material S6 for parameter details). Both benchmark results indicate that amorphous sputtered WTe₂ is a competitive SOT source in the emergent chalcogenide materials category.

E. Co-sputtered W_{100-x}Te_x devices

Lastly, we turn our focus on the possible origins of SOT in the amorphous WTe₂ heterostructures. Due to the lack of crystalline phase (and therefore no TSS) in our sample, we speculate that the SOC should have a bulk origin and the concentration of constituent elements will strongly affect ξ_{DL} . Figure 5(a) shows ξ_{DL} obtained from a series of co-sputtered samples, W_{100-x}Te_x(10)/CoTb(4.5)/Ta(2). It is found that $|\xi_{\text{DL}}|$ gradually increases and reaches a maximum at 18% of Te doping, where $\xi_{\text{DL}}^{\text{W}_{82}\text{Te}_{18}} \approx -0.09$. Further increasing the Te

concentration will lead to a decrease of $|\xi_{\text{DL}}|$. Note that ξ_{DL} changes sign from co-sputtered $\text{W}_{100-x}\text{Te}_x/\text{CoTb}$ (negative) to WTe_2/CoTb (positive). This sign-change suggests that the governing SOC behind the W-rich and the Te-rich regimes could be different. Although there is few work discussing the SOC or SOT from pure Te, previous studies have pointed out that elements with p -orbitals are able to possess strong SOCs.⁵¹⁻⁵³ A recent first principles calculation also indicates the spin Hall conductivity (SHC) is sensitive to the Fermi energy of WTe_2 , where the sign of SHC could reverse in a narrow energy window.⁵⁴

To understand the possible difference in SOT generation from WTe_2 and $\text{W}_{100-x}\text{Te}_x$, we further examine the SOC layer thickness dependence of $|\xi_{\text{DL}}|$ from both type of samples. For the co-sputtered case, we use $\text{W}_{82}\text{Te}_{18}/\text{CoTb}$ as the representative sample due to its maximized efficiency. As summarized in Fig. 5(b), the co-sputtered $\text{W}_{82}\text{Te}_{18}$ and the stoichiometric WTe_2 cases have a drastically difference in SOC layer dependence. For the co-sputtered case, the thickness dependence of efficiency can be well fitted by the spin diffusion model $|\xi_{\text{DL}}(t_{\text{W}_{82}\text{Te}_{18}})| = |\xi_{\text{DL}}^{\text{W}_{82}\text{Te}_{18}}| \left[1 - \text{sech}(t_{\text{W}_{82}\text{Te}_{18}} / \lambda_s^{\text{W}_{82}\text{Te}_{18}}) \right]$ ³³, with $|\xi_{\text{DL}}^{\text{W}_{82}\text{Te}_{18}}| \approx 0.09$ and spin diffusion length $\lambda_s^{\text{W}_{82}\text{Te}_{18}} \approx 4.1$ nm, which suggests that the SOC within $\text{W}_{82}\text{Te}_{18}$ is of bulk origin (such as the SHE). This is perhaps due to a dominating contribution of the SHE from W in the W-rich regime. In contrast, for WTe_2 , $|\xi_{\text{DL}}^{\text{WTe}_2}|$ decays with increasing the stoichiometric layer thickness, which indicates the possible existence of interfacial contributions of SOC besides the bulk effect.^{14,29} We speculate that interfacial effects could play crucial roles on the SOT generation in the Te-rich (stoichiometric) regime, even if the TMD layer is amorphous. Further studies are required to elucidate the SOC and SOT generation mechanisms in these amorphous TMD systems.

IV. Conclusions

In summary, we use conventional magnetron sputtering to deposit WTe₂ instead of mechanical exfoliation, where the structure is confirmed to be amorphous by TEM imaging. From the ST-FMR measurements, we obtain a sizable DL-SOT response with a low damping constant in WTe₂/CoFeB heterostructure ($\alpha_{\text{WTe}_2/\text{CoFeB}} \approx 0.01$). Through hysteresis loop shift measurements, the largest DL-SOT efficiency of WTe₂/CoTb heterostructure is characterized to be $\xi_{\text{DL}}^{\text{WTe}_2} \approx 0.20$. This large charge-to-spin conversion efficiency is further verified by current-induced magnetization switching with a low critical switching current density of $J_c \approx 7.05 \times 10^9 \text{ A/m}^2$. By comparing the stoichiometric WTe₂ to the co-sputtered W_{100-x}Te_x-based devices, the sign and magnitude of ξ_{DL} is found to be strongly composition dependent. Moreover, not only bulk SHE but also other interfacial SOC may contribute to the SOTs from WTe₂. Our observation therefore suggests that the relative composition between W and Te is the key factor, rather than the crystallinity, to affect the resulting spin transport properties, and the transport mechanism in amorphous sputtered WTe₂ can be described by the SPH model. With the features of wide-range tunable ξ_{DL} , low α , and low J_c , amorphous sputtered WTe₂ can serve as a potential SOT source material in the semiconducting regime.

Supplementary Material

See the supplementary material associated with this article.

Acknowledgements

We thank Tsao-Chi Chuang and Hsia-Ling Liang for the support on AFM and VSM measurements. We also thank Mr. Chung-Yuan Kao of Ministry of Science and Technology (National Taiwan University) for the assistance in EPMA, and thank Ms. Chia-Ying Chien of Ministry of Science and Technology (National Taiwan University) for the assistance on focused

ion beam (FIB). This work is supported by the Ministry of Science and Technology of Taiwan (MOST) under grant No. MOST-109-2636-M-002-006 and by the Center of Atomic Initiative for New Materials (AI-Mat) and the Advanced Research Center of Green Materials Science and Technology, National Taiwan University from the Featured Areas Research Center Program within the framework of the Higher Education Sprout Project by the Ministry of Education (MOE) in Taiwan under grant No. NTU-109L9008. The authors declare no competing financial interests.

Author Contributions

Cheng-Wei Peng prepared the IMA samples and performed ST-FMR measurement. Wei-Bang Liao prepared the PMA samples, performed hysteresis loop shift measurement and current-induced magnetization switching. Tian-Yue Chen conceived the experimental protocols and performed the analysis on the experimental data with Cheng-Wei Peng and Wei-Bang Liao. Chi-Feng Pai proposed and supervised the study.

Data availability

The data that support the findings of this study are available from the corresponding author upon reasonable request.

References

- ¹ Ioan Mihai Miron, Kevin Garello, Gilles Gaudin, Pierre-Jean Zermatten, Marius V. Costache, Stéphane Auffret, Sébastien Bandiera, Bernard Rodmacq, Alain Schuhl, and Pietro Gambardella, "Perpendicular switching of a single ferromagnetic layer induced by in-plane current injection," *Nature* **476**, 189 (2011).

- ² Luqiao Liu, O. J. Lee, T. J. Gudmundsen, D. C. Ralph, and R. A. Buhrman, "Current-induced switching of perpendicularly magnetized magnetic layers using spin torque from the spin Hall effect," *Phys. Rev. Lett.* **109**, 096602 (2012).
- ³ Murat Cubukcu, Olivier Boulle, Marc Drouard, Kevin Garello, Can Onur Avci, Ioan Mihai Miron, Juergen Langer, Berthold Ocker, Pietro Gambardella, and Gilles Gaudin, "Spin-orbit torque magnetization switching of a three-terminal perpendicular magnetic tunnel junction," *Appl. Phys. Lett.* **104**, 042406 (2014).
- ⁴ Sabpreet Bhatti, Rachid Sbiaa, Atsufumi Hirohata, Hideo Ohno, Shunsuke Fukami, and S. N. Piramanayagam, "Spintronics based random access memory: a review," *Mater. Today* **20**, 530 (2017).
- ⁵ Luqiao Liu, Chi-Feng Pai, Y. Li, H. W. Tseng, D. C. Ralph, and R. A. Buhrman, "Spin-torque switching with the giant spin Hall effect of tantalum," *Science* **336**, 555 (2012).
- ⁶ Chi-Feng Pai, Luqiao Liu, Y. Li, H. W. Tseng, D. C. Ralph, and R. A. Buhrman, "Spin transfer torque devices utilizing the giant spin Hall effect of tungsten," *Appl. Phys. Lett.* **101**, 122404 (2012).
- ⁷ Ting-Chien Wang, Tian-Yue Chen, Chun-Te Wu, Hung-Wei Yen, and Chi-Feng Pai, "Comparative study on spin-orbit torque efficiencies from W/ferromagnetic and W/ferrimagnetic heterostructures," *Phys. Rev. Mater.* **2**, 014403 (2018).
- ⁸ Wei-Bang Liao, Tian-Yue Chen, Yari Ferrante, Stuart S. P. Parkin, and Chi-Feng Pai,

- "Current-induced magnetization switching by the high spin Hall conductivity α -W," *Phys. Status Solidi RRL* **13**, 1900408 (2019).
- ⁹ Qiang Hao, Wenzhe Chen, and Gang Xiao, "Beta (β) tungsten thin films: Structure, electron transport, and giant spin Hall effect," *Appl. Phys. Lett.* **106**, 182403 (2015).
- ¹⁰ J. E. Hirsch, "Spin Hall effect," *Phys. Rev. Lett.* **83**, 1834 (1999).
- ¹¹ A. Hoffmann, "Spin Hall effects in metals," *IEEE Transactions on Magnetics* **49**, 5172 (2013).
- ¹² A. R. Mellnik, J. S. Lee, A. Richardella, J. L. Grab, P. J. Mintun, M. H. Fischer, A. Vaezi, A. Manchon, E. A. Kim, N. Samarth, and D. C. Ralph, "Spin-transfer torque generated by a topological insulator," *Nature* **511**, 449 (2014).
- ¹³ Jiahao Han, A. Richardella, Saima A. Siddiqui, Joseph Finley, N. Samarth, and Luqiao Liu, "Room-temperature spin-orbit torque switching induced by a topological insulator," *Phys. Rev. Lett.* **119**, 077702 (2017).
- ¹⁴ Yi Wang, Dapeng Zhu, Yang Wu, Yumeng Yang, Jiawei Yu, Rajagopalan Ramaswamy, Rahul Mishra, Shuyuan Shi, Mehrdad Elyasi, Kie-Leong Teo, Yihong Wu, and Hyunsoo Yang, "Room temperature magnetization switching in topological insulator-ferromagnet heterostructures by spin-orbit torques," *Nat. Commun.* **8**, 1364 (2017).
- ¹⁵ Mahendra Dc, Roberto Grassi, Jun-Yang Chen, Mahdi Jamali, Danielle Reifsnyder Hickey, Delin Zhang, Zhengyang Zhao, Hongshi Li, P. Quarterman, Yang Lv, Mo Li, Aurelien

- Manchon, K. Andre Mkhoyan, Tony Low, and Jian-Ping Wang, "Room-temperature high spin-orbit torque due to quantum confinement in sputtered $\text{Bi}_x\text{Se}_{(1-x)}$ films," *Nat. Mater.* **17**, 800 (2018).
- ¹⁶ Nguyen Huynh Duy Khang, Yugo Ueda, and Pham Nam Hai, "A conductive topological insulator with large spin Hall effect for ultralow power spin-orbit torque switching," *Nat. Mater.* **17**, 808 (2018).
- ¹⁷ Yabin Fan, Pramey Upadhyaya, Xufeng Kou, Murong Lang, So Takei, Zhenxing Wang, Jianshi Tang, Liang He, Li-Te Chang, Mohammad Montazeri, Guoqiang Yu, Wanjun Jiang, Tianxiao Nie, Robert N. Schwartz, Yaroslav Tserkovnyak, and Kang L. Wang, "Magnetization switching through giant spin-orbit torque in a magnetically doped topological insulator heterostructure," *Nat. Mater.* **13**, 699 (2014).
- ¹⁸ Tian-Yue Chen, Cheng-Wei Peng, Tsung-Yu Tsai, Wei-Bang Liao, Chun-Te Wu, Hung-Wei Yen, and Chi-Feng Pai, "Efficient spin-orbit torque switching with nonepitaxial chalcogenide heterostructures," *ACS Appl. Mater. Interfaces* **12**, 7788 (2020).
- ¹⁹ Tenghua Gao, Yuya Tazaki, Akio Asami, Hiroki Nakayama, and Kazuya Ando, "Semi-metallic bulk generated spin-orbit torques in disordered topological insulator," arXiv e-prints, arXiv:1911.00413 (2019).
- ²⁰ Zhendong Chi, Yong-Chang Lau, Xiandong Xu, Tadakatsu Ohkubo, Kazuhiro Hono, and Masamitsu Hayashi, "The spin Hall effect of Bi-Sb alloys driven by thermally excited Dirac-

- like electrons," *Sci. Adv.* **6**, eaay2324 (2020).
- ²¹ Qiming Shao, Guoqiang Yu, Yann-Wen Lan, Yumeng Shi, Ming-Yang Li, Cheng Zheng, Xiaodan Zhu, Lain-Jong Li, Pedram Khalili Amiri, and Kang L. Wang, "Strong Rashba-Edelstein effect-induced spin-orbit torques in monolayer transition metal dichalcogenide/ferromagnet bilayers," *Nano Lett.* **16**, 7514 (2016).
- ²² D. MacNeill, G. M. Stiehl, M. H. D. Guimaraes, R. A. Buhrman, J. Park, and D. C. Ralph, "Control of spin-orbit torques through crystal symmetry in WTe_2 /ferromagnet bilayers," *Nat. Phys.* **13**, 300 (2017).
- ²³ David MacNeill, Gregory M. Stiehl, Marcos H. D. Guimarães, Neal D. Reynolds, Robert A. Buhrman, and Daniel C. Ralph, "Thickness dependence of spin-orbit torques generated by WTe_2 ," *Phys. Rev. B* **96**, 054450 (2017).
- ²⁴ Weiming Lv, Zhiyan Jia, Bochong Wang, Yuan Lu, Xin Luo, Baoshun Zhang, Zhongming Zeng, and Zhongyuan Liu, "Electric-field control of spin-orbit torques in WS_2 /permalloy bilayers," *ACS Appl. Mater. Interfaces* **10**, 2843 (2018).
- ²⁵ Marcos H. D. Guimarães, Gregory M. Stiehl, David MacNeill, Neal D. Reynolds, and Daniel C. Ralph, "Spin-orbit torques in $NbSe_2$ /permalloy bilayers," *Nano Lett.* **18**, 1311 (2018).
- ²⁶ Peng Li, Weikang Wu, Yan Wen, Chenhui Zhang, Junwei Zhang, Senfu Zhang, Zhiming Yu, Shengyuan A. Yang, A. Manchon, and Xi-xiang Zhang, "Spin-momentum locking and spin-orbit torques in magnetic nano-heterojunctions composed of Weyl semimetal WTe_2 ," *Nat.*

- Commun. **9**, 3990 (2018).
- ²⁷ Shuyuan Shi, Shiheng Liang, Zhifeng Zhu, Kaiming Cai, Shawn D. Pollard, Yi Wang, Junyong Wang, Qisheng Wang, Pan He, Jiawei Yu, Goki Eda, Gengchiao Liang, and Hyunsoo Yang, "All-electric magnetization switching and Dzyaloshinskii–Moriya interaction in WTe₂/ferromagnet heterostructures," Nat. Nanotechnol. **14**, 945 (2019).
- ²⁸ Gregory M. Stiehl, Ruofan Li, Vishakha Gupta, Ismail El Baggari, Shengwei Jiang, Hongchao Xie, Lena F. Kourkoutis, Kin Fai Mak, Jie Shan, Robert A. Buhrman, and Daniel C. Ralph, "Layer-dependent spin-orbit torques generated by the centrosymmetric transition metal dichalcogenide β -MoTe₂," Phys. Rev. B **100**, 184402 (2019).
- ²⁹ Hongjun Xu, Jinwu Wei, Hengan Zhou, Jiafeng Feng, Teng Xu, Haifeng Du, Congli He, Yuan Huang, Junwei Zhang, Yizhou Liu, Han-Chun Wu, Chenyang Guo, Xiao Wang, Yao Guang, Hongxiang Wei, Yong Peng, Wanjun Jiang, Guoqiang Yu, and Xiufeng Han, "High spin Hall conductivity in large-area type-II Dirac semimetal PtTe₂," Adv. Mater. **32**, 2000513 (2020).
- ³⁰ Fei Xue, Christoph Rohmann, Junwen Li, Vivek Amin, and Paul Haney, "Unconventional spin-orbit torque in transition metal dichalcogenide—ferromagnet bilayers from first-principles calculations," Phys. Rev. B **102**, 014401 (2020).
- ³¹ Bing Zhao, Bogdan Karpiak, Dmitrii Khokhriakov, Annika Johansson, Anamul Md Hoque, Xiaoguang Xu, Yong Jiang, Ingrid Mertig, and Saroj P. Dash, "Unconventional charge–spin

- conversion in Weyl-semimetal WTe₂," Adv. Mater. **32**, 2000818 (2020).
- ³² Yuting Liu and Qiming Shao, "Two-dimensional materials for energy-efficient spin-orbit torque devices," ACS Nano **14**, 9389 (2020).
- ³³ Luqiao Liu, Takahiro Moriyama, D. C. Ralph, and R. A. Buhrman, "Spin-torque ferromagnetic resonance induced by the spin Hall effect," Phys. Rev. Lett. **106**, 036601 (2011).
- ³⁴ Chi-Feng Pai, Maxwell Mann, Aik Jun Tan, and Geoffrey S. D. Beach, "Determination of spin torque efficiencies in heterostructures with perpendicular magnetic anisotropy," Phys. Rev. B **93**, 144409 (2016).
- ³⁵ Yihong Fan, Hongshi Li, Mahendra Dc, Thomas Peterson, Jacob Held, Protyush Sahu, Junyang Chen, Delin Zhang, Andre Mkhoyan, and Jian-Ping Wang, "Spin pumping and large field-like torque at room temperature in sputtered amorphous WTe_{2-x} films," APL Mater. **8**, 041102 (2020).
- ³⁶ Xiang Li, Peng Li, Vincent D. H. Hou, Mahendra Dc, Chih-Hung Nien, Fen Xue, Di Yi, Chong Bi, Chien-Min Lee, Shy-Jay Lin, Wilman Tsai, Yuri Suzuki, and Shan X. Wang, "Large and robust charge-to-spin conversion in sputtered Weyl semimetal WTe_x with structural disorder," arXiv e-prints, arXiv:2001.04054 (2020).
- ³⁷ Jyun-Hong Huang, Hsing-Hung Chen, Pang-Shiuan Liu, Li-Syuan Lu, Chien-Ting Wu, Cheng-Tung Chou, Yao-Jen Lee, Lain-Jong Li, Wen-Hao Chang, and Tuo-Hung Hou,

- "Large-area few-layer MoS₂ deposited by sputtering," *Mater. Res. Express* **3**, 065007 (2016).
- ³⁸ Nevill Francis Mott and Edward A Davis, *Electronic processes in non-crystalline materials*. (Clarendon press: Oxford, 1979).
- ³⁹ David D. Djayaprawira, Koji Tsunekawa, Motonobu Nagai, Hiroki Maehara, Shinji Yamagata, Naoki Watanabe, Shinji Yuasa, Yoshishige Suzuki, and Koji Ando, "230% room-temperature magnetoresistance in CoFeB / MgO / CoFeB magnetic tunnel junctions," *Appl. Phys. Lett.* **86**, 092502 (2005).
- ⁴⁰ S. Ikeda, K. Miura, H. Yamamoto, K. Mizunuma, H. D. Gan, M. Endo, S. Kanai, J. Hayakawa, F. Matsukura, and H. Ohno, "A perpendicular-anisotropy CoFeB–MgO magnetic tunnel junction," *Nat. Mater.* **9**, 721 (2010).
- ⁴¹ Chi-Feng Pai, Yongxi Ou, Luis Henrique Vilela-Leão, D. C. Ralph, and R. A. Buhrman, "Dependence of the efficiency of spin Hall torque on the transparency of Pt/ferromagnetic layer interfaces," *Phys. Rev. B* **92**, 064426 (2015).
- ⁴² Jinwu Wei, Congli He, Xiao Wang, Hongjun Xu, Yizhou Liu, Yao Guang, Caihua Wan, Jiafeng Feng, Guoqiang Yu, and Xiufeng Han, "Characterization of spin-orbit torque efficiency in magnetic heterostructures with perpendicular magnetic anisotropy via spin-torque ferromagnetic resonance," *Phys. Rev. Appl.* **13**, 034041 (2020).
- ⁴³ Kouta Kondou, Hiroaki Sukegawa, Shinya Kasai, Seiji Mitani, Yasuhiro Niimi, and YoshiChika Otani, "Influence of inverse spin Hall effect in spin-torque ferromagnetic

- resonance measurements," *Appl. Phys. Express* **9**, 023002 (2016).
- ⁴⁴ Atsushi Okada, Yutaro Takeuchi, Kaito Furuya, Chaoliang Zhang, Hideo Sato, Shunsuke Fukami, and Hideo Ohno, "Spin-pumping-free determination of spin-orbit torque efficiency from spin-torque ferromagnetic resonance," *Phys. Rev. Appl.* **12**, 014040 (2019).
- ⁴⁵ Keisuke Yamada, Kiyooki Oomaru, Satoshi Nakamura, Tomonori Sato, and Yoshinobu Nakatani, "Reducing the switching current with a Gilbert damping constant in nanomagnets with perpendicular anisotropy," *Appl. Phys. Lett.* **106**, 042402 (2015).
- ⁴⁶ Chih-Liang Wang, Sheng-Huang Huang, Chih-Huang Lai, Wei-Chuan Chen, Shan-Yi Yang, Kuei-Hung Shen, and Hui-Yun Bor, "Reduction in critical current density by tuning damping constants of CoFeB for spin-torque-transfer switching," *J. Phys. D: Appl. Phys.* **42**, 115006 (2009).
- ⁴⁷ P. Hansen, C. Clausen, G. Much, M. Rosenkranz, and K. Witter, "Magnetic and magneto-optical properties of rare-earth transition-metal alloys containing Gd, Tb, Fe, Co," *J. Appl. Phys.* **66**, 756 (1989).
- ⁴⁸ Joseph Finley and Luqiao Liu, "Spin-orbit-torque efficiency in compensated ferrimagnetic cobalt-terbium alloys," *Phys. Rev. Appl.* **6**, 054001 (2016).
- ⁴⁹ Satoru Emori, Eduardo Martinez, Kyung-Jin Lee, Hyun-Woo Lee, Uwe Bauer, Sung-Min Ahn, Parnika Agrawal, David C. Bono, and Geoffrey S. D. Beach, "Spin Hall torque magnetometry of Dzyaloshinskii domain walls," *Phys. Rev. B* **90**, 184427 (2014).

- ⁵⁰ O. J. Lee, L. Q. Liu, C. F. Pai, Y. Li, H. W. Tseng, P. G. Gowtham, J. P. Park, D. C. Ralph, and R. A. Buhrman, "Central role of domain wall depinning for perpendicular magnetization switching driven by spin torque from the spin Hall effect," *Phys. Rev. B* **89**, 024418 (2014).
- ⁵¹ X. Gonze, J. P. Michenaud, and J. P. Vigneron, "Ab initio calculations of bismuth properties, including spin-orbit coupling," *Phys. Scr.* **37**, 785 (1988).
- ⁵² Siqi Lin, Wen Li, Zhiwei Chen, Jiawen Shen, Binghui Ge, and Yanzhong Pei, "Tellurium as a high-performance elemental thermoelectric," *Nat. Commun.* **7**, 10287 (2016).
- ⁵³ Chang Niu, Gang Qiu, Yixiu Wang, Zhuocheng Zhang, Mengwei Si, Wenzhuo Wu, and Peide D. Ye, "Gate-tunable strong spin-orbit interaction in two-dimensional tellurium probed by weak antilocalization," *Phys. Rev. B* **101**, 205414 (2020).
- ⁵⁴ Jiaqi Zhou, Junfeng Qiao, Arnaud Bournel, and Weisheng Zhao, "Intrinsic spin Hall conductivity of the semimetals MoTe₂ and WTe₂," *Phys. Rev. B* **99**, 060408 (2019).

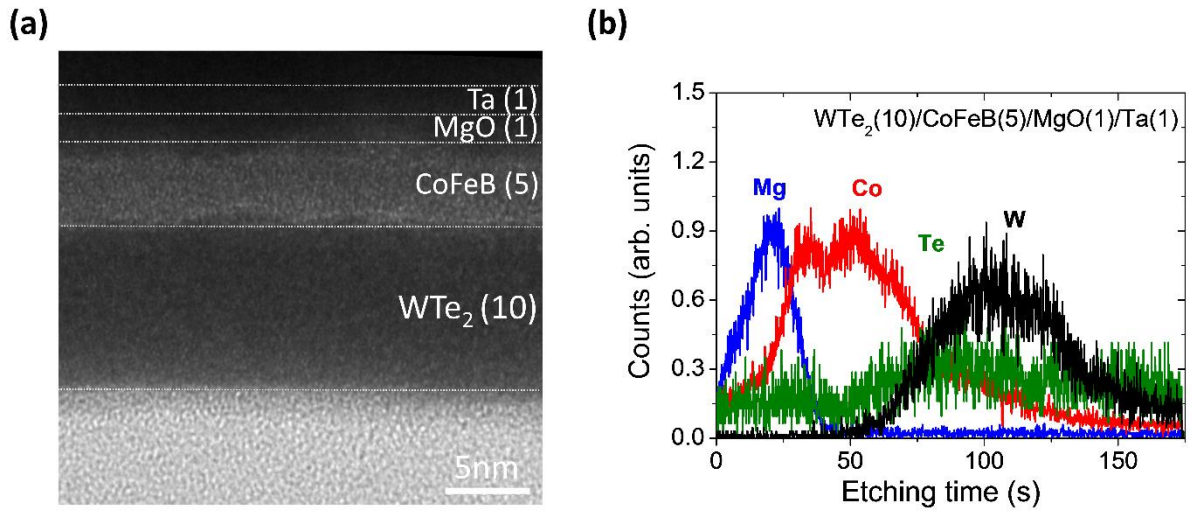


FIG. 1. Structural characterization of WTe₂-based heterostructure. (a) Cross-sectional TEM image and (b) SIMS signals with respect to the etching (Ar ion-milling) time of a representative WTe₂(10)/CoFeB(5)/MgO(1)/Ta(1) heterostructure.

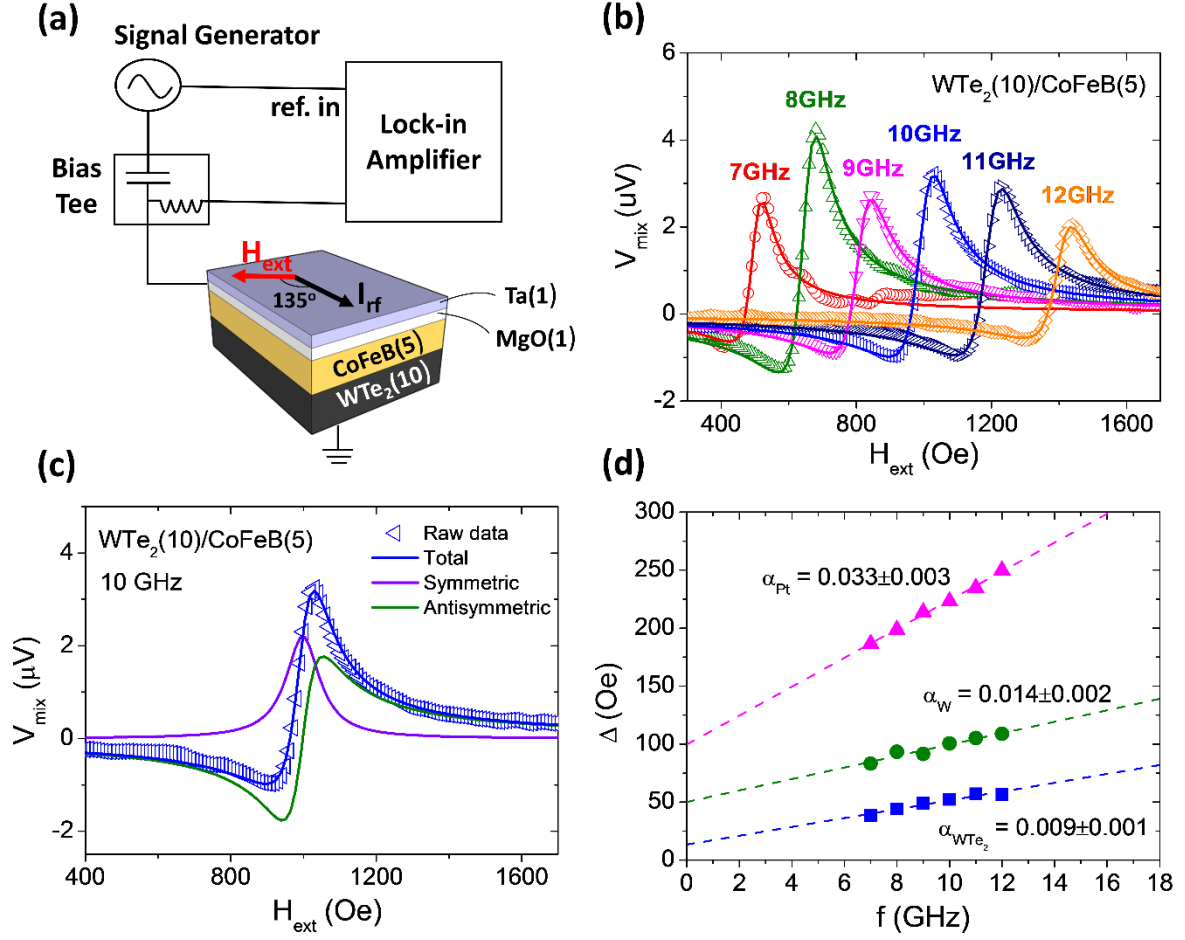


FIG. 2. ST-FMR measurement of $\text{WTe}_2(10)/\text{CoFeB}(5)/\text{MgO}(1)/\text{Ta}(1)$ device. (a) Illustration of ST-FMR measurements setup. (b) The ST-FMR spectra of a $\text{WTe}_2(10)/\text{CoFeB}(5)/\text{MgO}(1)/\text{Ta}(1)$ microstrip for $f = 7$ to 12 GHz. (c) Representative ST-FMR result of $\text{WTe}_2(10)/\text{CoFeB}(5)/\text{MgO}(1)/\text{Ta}(1)$ at $f = 10$ GHz. The raw data is fitted by the sum of a symmetric and an antisymmetric Lorentzian. (d) f dependence of linewidth Δ for $\text{Pt}(6)/\text{CoFeB}(5)/\text{MgO}(1)/\text{Ta}(1)$, $\text{W}(4)/\text{CoFeB}(5)/\text{MgO}(1)/\text{Ta}(1)$ and $\text{WTe}_2(10)/\text{CoFeB}(5)/\text{MgO}(1)/\text{Ta}(1)$ structures.

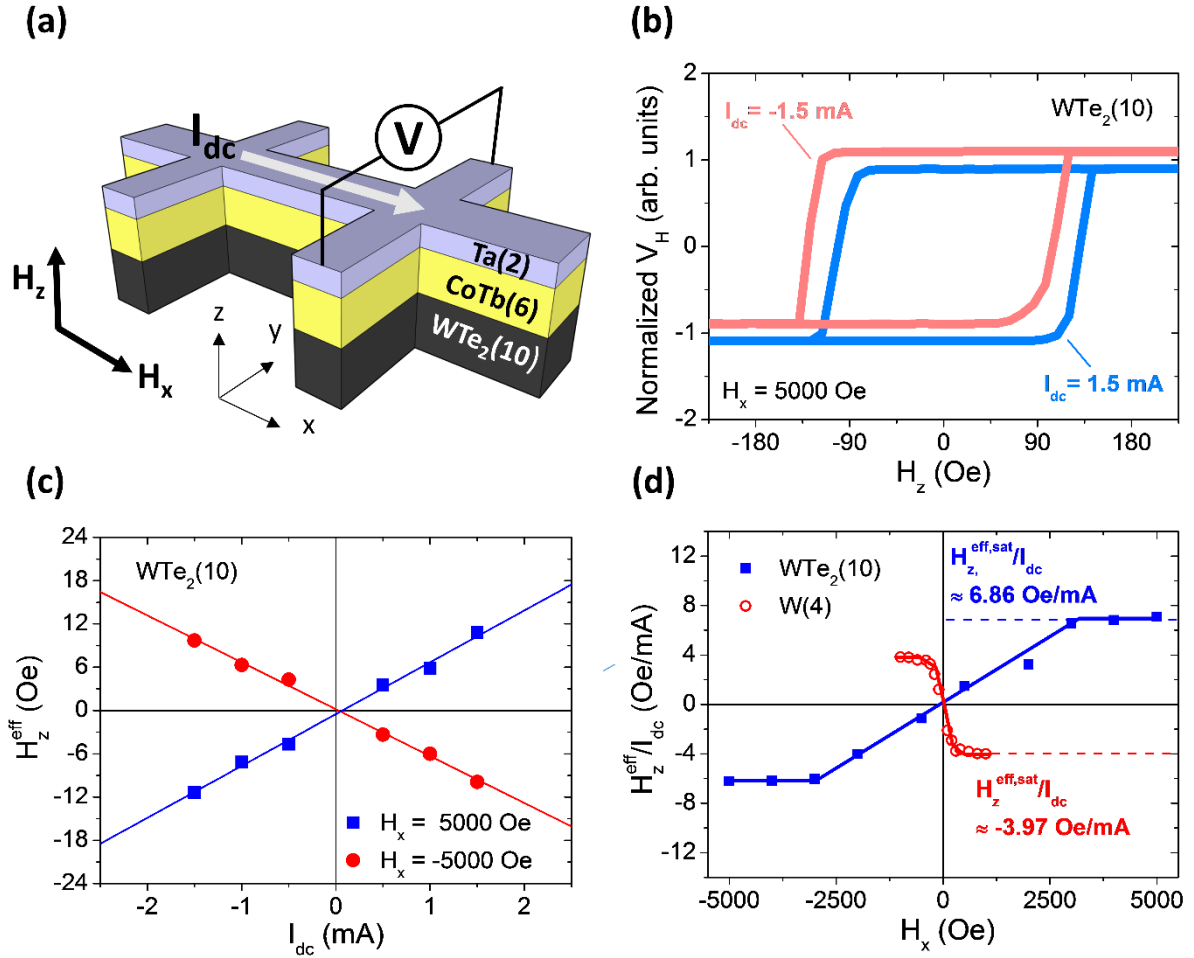


FIG. 3. Hysteresis loop shift measurement of $\text{WTe}_2(10)/\text{CoTb}(6)/\text{Ta}(2)$ device. (a) Illustration of a Hall bar device for hysteresis loop shift measurement. (b) Representative shifted hysteresis loops of a $\text{WTe}_2(10)/\text{CoTb}(6)/\text{Ta}(2)$ device with $I_{dc} = \pm 1.5$ mA and $H_x = 5000$ Oe. (c) The effective fields as functions of applied currents under $H_x = \pm 5000$ Oe. (d) H_z^{eff}/I_{dc} as functions of H_x for $\text{WTe}_2(10)/\text{CoTb}(6)/\text{Ta}(2)$ and $\text{W}(4)/\text{CoTb}(6)/\text{Ta}(2)$ (control) heterostructures.

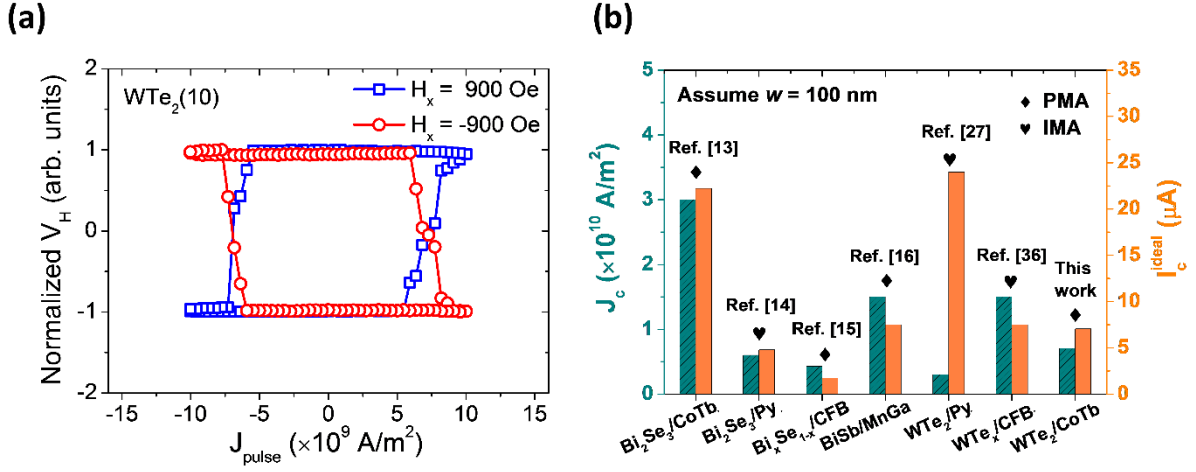


FIG. 4. Current-induced magnetization switching in $\text{WTe}_2(10)/\text{CoTb}(6)/\text{Ta}(2)$ device. (a) Current-induced magnetization switching from a $\text{WTe}_2(10)/\text{CoTb}(6)/\text{Ta}(2)$ device with applied bias fields $H_x = \pm 900 \text{ Oe}$. (b) Comparison of critical switching current density J_c (left y axis) and ideal critical switching current I_c^{ideal} (right y axis) among TIs and WTe_2 based heterostructures.

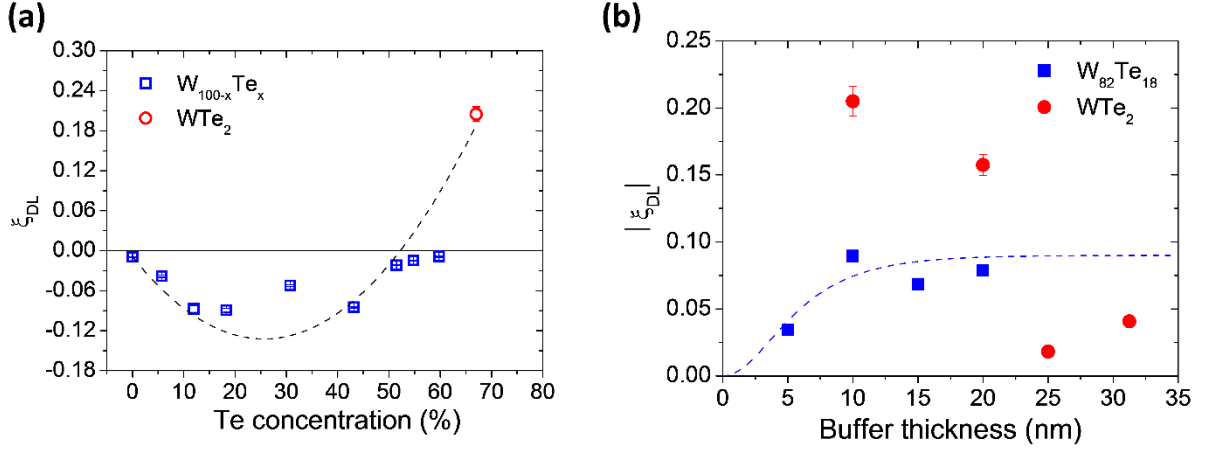


FIG. 5. Comparison of SOT from WTe_2 and co-sputtered $W_{100-x}Te_x$. (a) The DL-SOT efficiency ξ_{DL} of $W_{100-x}Te_x/CoTb$ heterostructures as a function of Te concentration. The blue open squares represent the devices with co-sputtered $W_{100-x}Te_x$, and the red open circle represents the stoichiometric WTe_2 case. The dashed line serves as guide to the eye. (b) Buffer layer thickness dependence of $|\xi_{DL}|$ for $W_{82}Te_{18}$ -based and WTe_2 -based devices. The blue dashed line represents the fitting of the $|\xi_{DL}(t_{W_{82}Te_{18}})|$ data to a spin diffusion model with spin diffusion length $\lambda_s^{W_{82}Te_{18}} \approx 4.1$ nm.